www.nature.com/cdd

CDDpress

ARTICLE

CD-NTase family member MB21D2 promotes cGAS-mediated antiviral and antitumor immunity

Hansen Liu[1,2,5], Zhenzhen Yan[1,2,5], Deyu Zhu[3,5], Haiyan Xu[3], Feng Liu[1,2], Tian Chen[4], Honghai Zhang[1,2], Yi Zheng[1,2], Bingyu Liu[1,2], Lei Zhang[1,2], Wei Zhao[1,4] and Chengjiang Gao[1,2]✉

cGAS/DncV-like nucleotidyltransferase (CD-NTase) family members are immune sensors that synthesize diverse nucleotide signals to initiate antiviral response in bacteria and animals. As a founding member of CD-NTase enzyme, cGAS has been identified as a key sensor for cytoplasmic DNA and type I interferons (IFNs) signaling in metazoan. However, the functions of other metazoan CD-NTases remain enigmatic. Here, we showed that Mab-21 domain-containing protein 2 (MB21D2), another member of the CD-NTase family, plays a positive role in modulating the cGAS-STING signaling in myeloid cells. Deficiency of MB21D2 in THP-1 cells or mice macrophages led to impaired production of type I interferon upon DNA stimulation. Consistently, *Mb21d2*$^{-/-}$ mice showed more susceptible to infection with DNA virus and faster growth of melanoma, compared to its counterparts. Mechanistically, MB21D2 specially bound with the N-terminal of cGAS, facilitated its liquid phase condensation and DNA-binding activity, leading to the enhanced production of cGAMP and subsequent IFN-β production. Thus, our findings unveiled that the CD-NTase family member MB21D2 contributes to host antiviral and antitumor responses by enhancing cGAS activation.

Cell Death & Differentiation (2023) 30:992–1004; https://doi.org/10.1038/s41418-023-01116-1

INTRODUCTION

The emergence of DNA in the cytoplasm is a danger signal for pathogen infection or tissue damage and triggers robust innate immune responses [1–3]. Cyclic GMP-AMP synthase (cGAS) is an important DNA sensor, which is responsible for mediating immune response upon cytoplasmic DNA challenge. After detection of intracellular DNA, cGAS triggers the synthesis of cyclic guanosine monophosphate (GTP)-adenosine monophosphate (ATP) (cGAMP) [1, 4]. cGAMP in turn acts as a second messenger to activate the endoplasmic reticulum (ER) membrane adapter protein STING and then activates downstream signal cascade to induce the expression of type I interferons (IFNs) [1, 5]. IFNs not only play central roles in host antiviral immunity [6], but are also essential for antitumor immunity [7].

cGAS is activated by direct recognition of double-stranded DNA (dsDNA) in a sequence-independent manner [1]. Binding to DNA induces a conformational change in the active site of cGAS, which is essential for its activation [1]. In the first step towards activation, cGAS interacts with DNA to form a 2:2 complex [8, 9]. cGAS dimers further assemble into oligomers, with unique biophysical properties of liquid-like droplets [10], which are observed as cytoplasmic foci within cells. The formation of cGAS condensates is indispensable for 2′, 3′-cGAMP synthesis and innate immune signaling [10, 11]. Long DNAs are more efficient in promoting cGAS enzymatic activity and liquid phase condensation than their shorter counterparts [10, 12, 13]. Recent work showed that G3BP1 [14] and RNA-dependent kinase PKR [15] are required for the formation of cGAS condensates. However, more details of the formation of cGAS condensates need to be further investigated.

A recent discovery of diverse structural homologs of cGAS reveals that cGAS belongs to the CD-NTase family [16] that synthesizes noncanonical RNA signals including cyclic dinucleotides, cyclic trinucleotides, and linear oligonucleotides. Except for cGAS, 2′–5′-oligoadenylate synthetases (OAS1/2/3) are important members of CD-NTase in *Homo sapiens*. OAS1 synthesizes 2′–5′-oligoadenylate after sensing cytosolic double-stranded RNA to induce RNA degradation by activating RNaseL [17]. OASL is a catalytically inactive member of OASs. OASL harbors the N-terminal OAS-like domain, but the NTase domain is changed in the active site. Some studies showed that OASL functions as a cofactor to modulate cellular RNA sensing [18]. Moreover, OASL directly and specifically binds to cGAS independently of double-stranded DNA, resulting in a non-competitive inhibition of the second messenger cGAMP production [19]. Except for cGAS and OAS, there are nine enzymes in the human genome that belong to the CD-NTase family [20]. However, the function of these enzymes in host immunity remains elusive.

Here, we reported a role for Mab-21 domain-containing protein 2 (MB21D2) in promoting antiviral and antitumor immunity through interacting with cGAS. MB21D2 promotes the liquid phase condensation and DNA-binding activity of cGAS, and facilitates the production of cGAMP. Knockdown of MB21D2 in THP-1 cells, as well as mice macrophages derived from *Mb21d2*$^{-/-}$ mice, showed decreased DNA-induced IFN-β production.

[1]Key Laboratory of Infection and Immunity of Shandong Province & Key Laboratory for Experimental Teratology of Ministry of Education, Shandong University, Jinan, Shandong 250012, PR China. [2]Department of Immunology, School of Biomedical Sciences, Shandong University, Jinan, Shandong 250012, PR China. [3]Department of Biochemistry and Molecular Biology, School of Biomedical Sciences, Shandong University, Jinan, Shandong 250012, PR China. [4]Department of Pathogenic Biology, School of Biomedical Sciences, Shandong University, Jinan, Shandong 250012, PR China. [5]These authors contributed equally: Hansen Liu, Zhenzhen Yan, Deyu Zhu. ✉email: cgao@sdu.edu.cn

Received: 11 April 2022 Revised: 6 January 2023 Accepted: 11 January 2023
Published online: 21 January 2023

Consistently, bone marrow chimeric mice WT/BMT-*Mb21d2*$^{-/-}$ mice (transplantation of *Mb21d2*$^{-/-}$ bone marrow to irradiated WT mice) showed enhanced virus replication and faster growth of melanoma than WT/BMT-WT mice (transplantation of WT bone marrow to irradiated WT mice).

RESULTS

MB21D2 positively regulates cGAS-mediated IFN-β production

cGAS belongs to the CD-NTase family, which is composed of several members with a common structural architecture in human genome. To investigate whether other CD-NTase family members have a similar function as cGAS in immune response, we cloned seven members of CD-NTase enzymes and transfected them together with STING into HEK293T cells. We found only cGAS could stimulate STING-mediated IFN-β expression (Supplementary Fig. S1A, B). Other CD-NTases, including its closest homolog MB21D2 could not promote STING-mediated IFN-β expression (Supplementary Fig. S1B). We then transfected each CD-NTase enzyme together with cGAS and STING into HEK293T cells, and found that MB21D2 promoted cGAS/STING-mediated IFN-β expression, while OASL showed an opposite effect as reported [19] (Supplementary Fig. S1C). Western blot analysis showed that MB21D2 was expressed in various organs with the highest expression in the brain (Supplementary Fig. S1D). These data suggested that MB21D2 may regulate cGAS-induced IFN-β signaling.

To investigate the function of MB21D2 in host immunity, we transfected MB21D2 siRNA into THP-1 cells to knockdown MB21D2 expression (Supplementary Fig. S2A), followed by transfection with ISD (Immune Stimulatory DNA, a 45-bp DNA oligo), or cGAMP, or infection with HSV-1. We found the mRNA expression level of *IFNB1* and the secretion level of IFN-β were significantly decreased in MB21D2 knockdown cells upon stimulation with ISD, or infection with HSV-1 (Supplementary Fig. S2B, C). However, MB21D2 knockdown did not affect the *IFNB1* expression or IFN-β secretion upon cGAMP stimulation in THP-1 cells (Supplementary Fig. S2B, C). Consistently, we found the expression of *CCL5* and *CXCL10*, downstream genes of *IFNB1*, was attenuated in MB21D2 knockdown cells upon ISD stimulation or HSV-1 infection, but not cGAMP stimulation (Supplementary Fig. S2B).

To confirm the function of MB21D2 in IFN-β signaling, we used CRSPR/Cas9 technique to knockout MB21D2 in HeLa cells (Supplementary Fig. S2D). Compared with wild-type (sg Ctrl) HeLa cells, we found the expression of *IFNB1* in *MB21D2* KO (sg KO) cells was significantly decreased after ISD stimulation or HSV-1 infection (Fig. 1A). Reintroduction of MB21D2 into sg KO cells restored the ISD- or HSV-1-induced *IFNB1* production (Fig. 1A). However, there was no significant difference in cGAMP- or SeV-induced *IFNB1* expression between sg Ctrl cells and sg KO cells (Fig. 1A). We further showed that overexpression of MB21D2 in HeLa cells increased the ISD- or HSV-1-induced expression of *IFNB1* (Supplementary Fig. S2E).

To investigate the function of MB21D2 in different species, we constructed *Mb21d2*$^{-/-}$ mice and isolated peritoneal macrophages from WT and *Mb21d2*$^{-/-}$ mice, followed by stimulation with ISD, or cGAMP, or infection with HSV-1. We found the expression of *Ifnb1* and the secretion of IFN-β were decreased in *Mb21d2*$^{-/-}$ macrophages upon ISD stimulation or HSV-1 infection, but not cGAMP stimulation (Fig. 1B, C). The expression of *Mx-1*, *Isg-15*, *Ccl5* and *Cxcl10*, downstream genes of *Ifnb1*, was also lower in *Mb21d2*$^{-/-}$ macrophages than its counterparts after stimulation with ISD, or infection with HSV-1 (Fig. 1D). Moreover, we prepared Mouse Embryonic Fibroblasts (MEFs) from WT and *Mb21d2*$^{-/-}$ mice, and found MB21D2 deficiency decreased the expression of *Ifnb1* upon stimulated with ISD or infected with HSV-1, and reintroduction of MB21D2 restored the *Ifnb1* expression (Fig. 1E). However, MB21D2 deficiency did not affect the *Ifnb1* level after cGAMP stimulation, or SeV infection in MEFs (Fig. 1E). Then, we measured the expression of MB21D2 upon HSV-1 infection in various macrophages or dendritic cells (DCs). We found DNA virus infection did not affect the protein level of MB21D2 (Supplementary Fig. S3A). Taken together, these data demonstrated that MB21D2 regulates cGAS-induced IFN-β production upon DNA stimulation.

MB21D2 positively regulates cGAS-mediated innate signaling

Following DNA recognition, cGAS catalyzes the formation of cGAMP, which stimulates the activation of STING and subsequently activates TBK1 and IRF3, leading to the production of downstream IFNs. We measured the effect of MB21D2 on cGAS-mediated IFN-β signaling. Western blot analysis showed that the phosphorylation of STING, TBK1 and IRF3 was increased upon ISD stimulation or HSV-1 infection in mice macrophages, while MB21D2 deficiency attenuated phosphorylation of STING, TBK1 and IRF3 (Fig. 2A and Supplementary Fig. S4A). However, cGAMP-induced phosphorylation of STING, TBK1 and IRF3 were not impaired in MB21D2 deficient mice macrophages, compared to its counterparts (Fig. 2A and Supplementary Fig. S4A). Consistently, siRNA knockdown of MB21D2 expression also attenuated the phosphorylation of STING, TBK1 and IRF3 upon ISD stimulation and HSV-1 infection, but not cGAMP stimulation in THP-1 cells (Supplementary Fig. S3B). In addition, we used *MB21D2* sg KO HeLa cells to perform these experiments. We found the phosphorylation of TBK1 and IRF3 was lower in sg KO cells than sg Ctrl cells after stimulation with ISD or infection with HSV-1 (Fig. 2B and Supplementary Fig. S4B). More importantly, we found the phosphorylation of TBK1 and IRF3 was restored after MB21D2 reintroduction in sg KO cells (Fig. 2B and Supplementary Fig. S4B). However, cGAMP-induced phosphorylation of TBK1 and IRF3 was not impaired in MB21D2 deficient HeLa cells (Fig. 2B and Supplementary Fig. S4B). Further, we found that the phosphorylation of TBK1 and IRF3 was higher in MB21D2-overexpressed HeLa cells, compared with its counterparts, upon ISD stimulation, or HSV-1 infection (Supplementary Fig. S3C). IRF3 has been reported to form a homodimer after phosphorylation and then move to the nucleus [21]. Western blot analysis and microscopy results showed that the nuclear translocation of IRF3 was lower in sg KO HeLa cells, *Mb21d2*$^{-/-}$ MEFs and macrophages than their counterparts after ISD stimulation (Fig. 2C, D and Supplementary Fig. S3D). Together, these data indicated that MB21D2 positively regulates the cGAS-mediated innate signaling to regulate IFN-β production.

MB21D2 interacts with cGAS

Given the above data that MB21D2 regulates IFN-β signaling with ISD transfection and HSV-1 infection, but not cGAMP transfection, we inferred that MB21D2 may target cGAS. To determine whether MB21D2 promoted the immune response through cGAS, we measured the interaction between these two proteins. We transfected MB21D2 expression plasmid together with various expression plasmids in the IFN-β signaling pathway, including cGAS, STING, MAVS, RIG-I, TBK1 and IRF3 into HEK293T cells. Coimmunoprecipitation and western blotting showed that MB21D2 could interact specifically with cGAS, instead of STING, MAVS, RIG-I, TBK1 or IRF3 (Fig. 3A). Endogenous MB21D2 and cGAS were coimmunoprecipitated in THP-1 cells, and their interaction was enhanced upon ISD stimulation (Fig. 3B, Supplementary Fig. S4C). Next, we transfected cGAS and MB21D2 into HeLa cells and measured the colocalization of these two proteins. Confocal microscope images showed that MB21D2 colocalized with cGAS (Fig. 3C). Similarly, ISD stimulation increased the colocalization between cGAS and MB21D2 with a characteristic puncta structure (Fig. 3C). To exclude the possibility that DNA affect the interaction between cGAS and MB21D2, we added DNase I to the IP reaction. We found that DNase I do not affect the interaction between cGAS and MB21D2 (Supplementary Fig. S5A), indicating the interaction between cGAS and MB21D2 is not

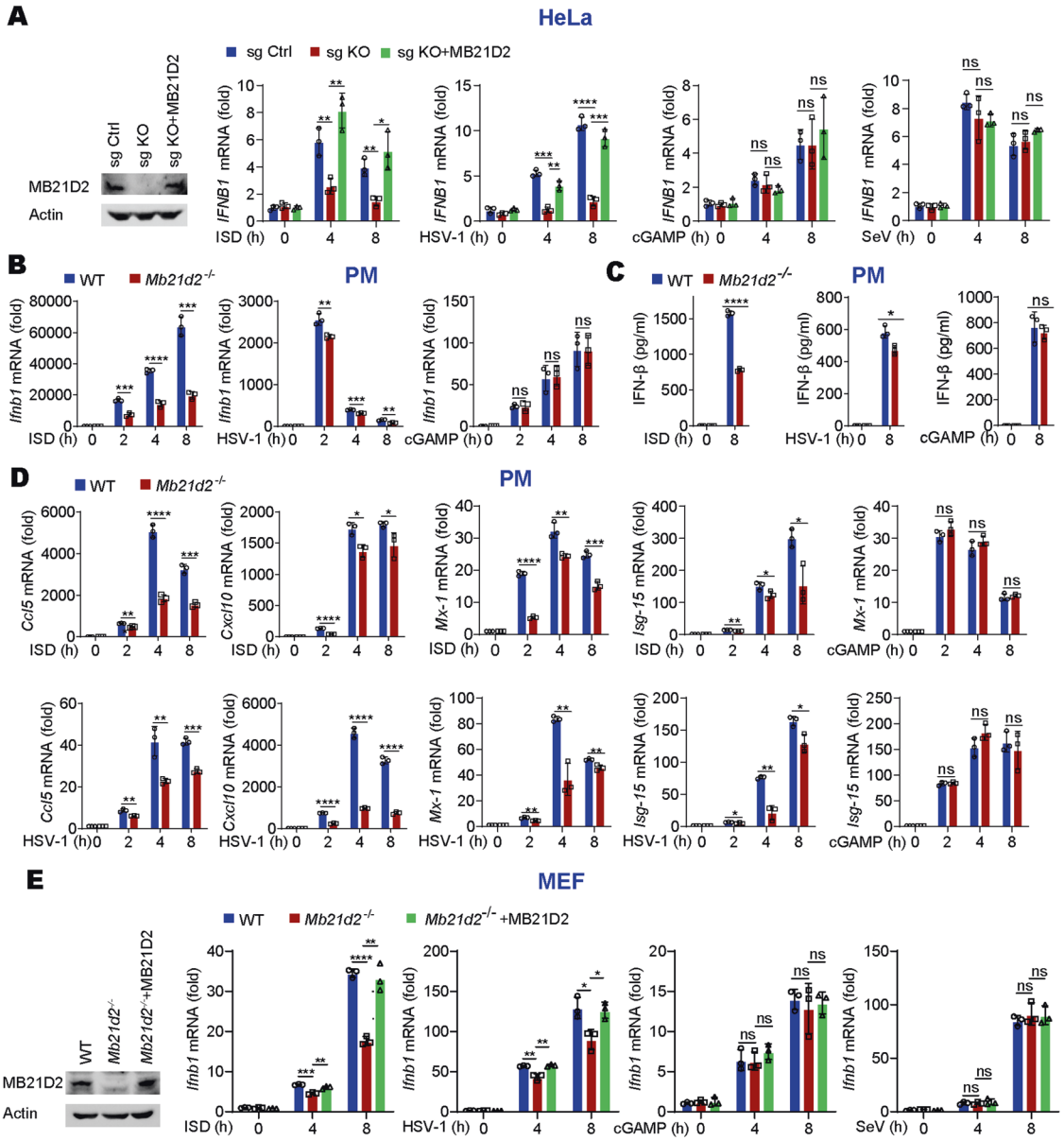

Fig. 1 MB21D2 facilitates cGAS-mediated IFN-β production. A sg Ctrl, sg KO, or sg KO reintroduced of MB21D2 HeLa cells were stimulated with ISD or cGAMP, or infected with HSV-1 or SeV for indicated times. Expression of *IFNB1* mRNA was measured by RT-PCR, $n = 3$. **B** WT or *Mb21d2*$^{-/-}$ peritoneal macrophages were stimulated with ISD or cGAMP, or infected with HSV-1 for indicated times. Expression of *Ifnb1* mRNA was measured by RT-PCR, $n = 3$. **C** WT or *Mb21d2*$^{-/-}$ peritoneal macrophages were stimulated with ISD or cGAMP, or infected with HSV-1 for 8 h. The IFN-β secretion level was measured by ELISA, $n = 3$. **D** WT or *Mb21d2*$^{-/-}$ peritoneal macrophages were stimulated with ISD or cGAMP, or infected with HSV-1 for indicated times. Expression of *Mx-1*, *Isg-15*, *Ccl5 and Cxcl10* mRNA was measured by RT-PCR, $n = 3$. **E** WT, *Mb21d2*$^{-/-}$ or *Mb21d2*$^{-/-}$ reintroduced of MB21D2 MEFs were stimulated with ISD or cGAMP, or infected with HSV-1 or SeV for indicated times. The protein level of MB21D2 was measured by Western blot. Expression of *Ifnb1* mRNA was measured by RT-PCR, $n = 3$. Data are shown as mean ± SD and were analyzed by unpaired two-tailed Student's *t* test (**A**–**E**) (*$p < 0.05$, **$p < 0.01$, ***$p < 0.001$, ****$p < 0.0001$).

mediated by both of the proteins binding to DNA. Moreover, in vitro Pull-Down assays with recombinant proteins showed that human cGAS full length (hcGAS FL) bound to MB21D2 directly (Fig. 3D), while the hcGAS-ΔN Mutant (residues 161–522) could not (Fig. 3D). Similarly, we found mouse cGAS full length (mcGAS FL), but not the mcGAS-ΔN Mutant (residues 147–507) bound to MB21D2 (Fig. 3E). These data indicated that MB21D2 binds to the N-terminal region of cGAS.

To identify the key domain of MB21D2 responsible for its interaction with cGAS, we prepared recombinant full-length MB21D2 and a MB21D2 deletion Mutant (residues 26–428), which harbors the hypothetical enzyme activity domain according to the structure of cGAS. In vitro Pull-Down assays showed that MB21D2 full length bound to mcGAS, whereas the MB21D2 deletion Mutant could not (Fig. 3F), indicating that the residues 1–25 and 429–491 of MB21D2 were important for its binding with cGAS. Together, these data demonstrated that MB21D2 physically interacts with cGAS to promote cGAS-mediated innate signaling and IFN-β production.

MB21D2 promotes the DNA-binding affinity of cGAS

We investigated whether MB21D2 promoted the DNA-binding activity of cGAS. Firstly, we transfected Myc-MB21D2 and Myc-cGAS individually into HEK293T cells for 24 h, followed by

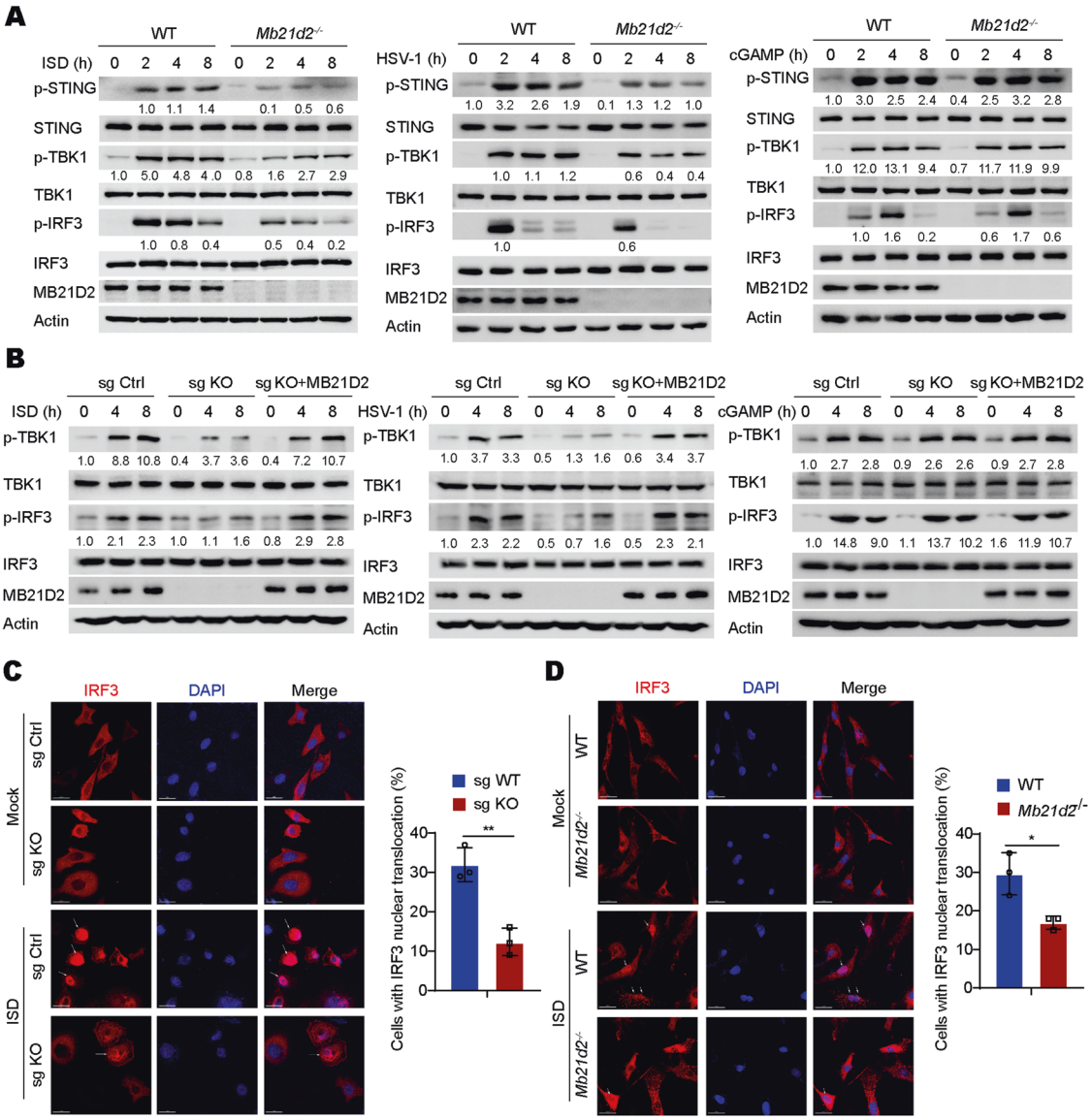

Fig. 2 MB21D2 facilitates cGAS-mediated IFN-β signaling. A Western blot analysis of p-STING, p-TBK1 and p-IRF3 in WT and *Mb21d2*$^{-/-}$ peritoneal macrophages after ISD or cGAMP stimulation, or HSV-1 infection for indicated times. **B** Western blot analysis of p-TBK1 and p-IRF3 in sg Ctrl, sg KO, and sg KO reintroduced of MB21D2 HeLa cells after ISD or cGAMP stimulation, or HSV-1 infection for indicated times. **C** Microscopy images of IRF3 nuclear translocation in sg Ctrl or sg KO HeLa cells after ISD stimulation for 4 h (left). The percentage of cells with nuclear translocation was quantified (right), at least 100 cells from each group were analyzed, $n = 3$. Scale bar, 20 μm. **D** Microscopy images of IRF3 nuclear translocation in WT or *Mb21d2*$^{-/-}$ MEFs after ISD stimulation for 4 h (left). The percentage of cells with nuclear translocation was quantified (right), at least 100 cells from each group were analyzed, $n = 3$. Scale bar, 20 μm. Data are shown as mean ± SD and were analyzed by unpaired two-tailed Student's *t* test (**C**, **D**) (*$p < 0.05$, **$p < 0.01$).

transfection with Biotin-ISD for 4 h. Streptavidin Pull-Down assays revealed that cGAS bound to Biotin-ISD, while MB21D2 could not (Supplementary Fig. S5B). Microscopy images showed that the fluorescence of Myc-cGAS merged with CY3-ISD foci (Supplementary Fig. S5C). However, MB21D2 alone could neither merge with CY3-ISD nor form foci in the cytoplasm as cGAS (Supplementary Fig. S5C). Notably, when Myc-MB21D2 and Flag-cGAS were transfected together into HEK293T cells for 24 h, followed by Biotin-ISD treatment for 4 h, we found that the binding of cGAS to Biotin-ISD was greatly increased in the presence of MB21D2 (Fig. 4A). In vitro Pull-Down assays with recombinant proteins further confirmed that the binding of hcGAS to Biotin-ISD was increased in the presence of MB21D2 (Fig. 4B). In addition, we transfected Myc-cGAS into HeLa cells, followed by transfection of CY3-ISD and monitored the colocalization of Myc-cGAS with CY3-ISD. Microscopy images showed that the fluorescence of Myc-cGAS merged with CY3-ISD foci (Fig. 4C), indicating the binding of cGAS to ISD in cells. Notably, we found the cGAS-DNA puncta were larger in MB21D2-overexpressed HeLa cells (Fig. 4C). Further, we measured the DNA-binding ability of mcGAS in peritoneal macrophages prepared from WT and *Mb21d2*$^{-/-}$ mice. Streptavidin Pull-Down assay showed that the binding between mcGAS and Biotin-ISD was greatly decreased in *Mb21d2*$^{-/-}$ mice macrophages, compared to its counterparts (Fig. 4D). Microscopy images showed that cGAS-ISD foci formation was attenuated in *Mb21d2*$^{-/-}$ macrophages, compared to WT mice macrophages (Fig. 4E). Consistently, we found that the DNA-binding efficiency of cGAS was also reduced in MB21D2 knockdown THP-1 cells upon ISD stimulation (Fig. 4F). Altogether, these data demonstrated that MB21D2 promotes the DNA-binding affinity of cGAS.

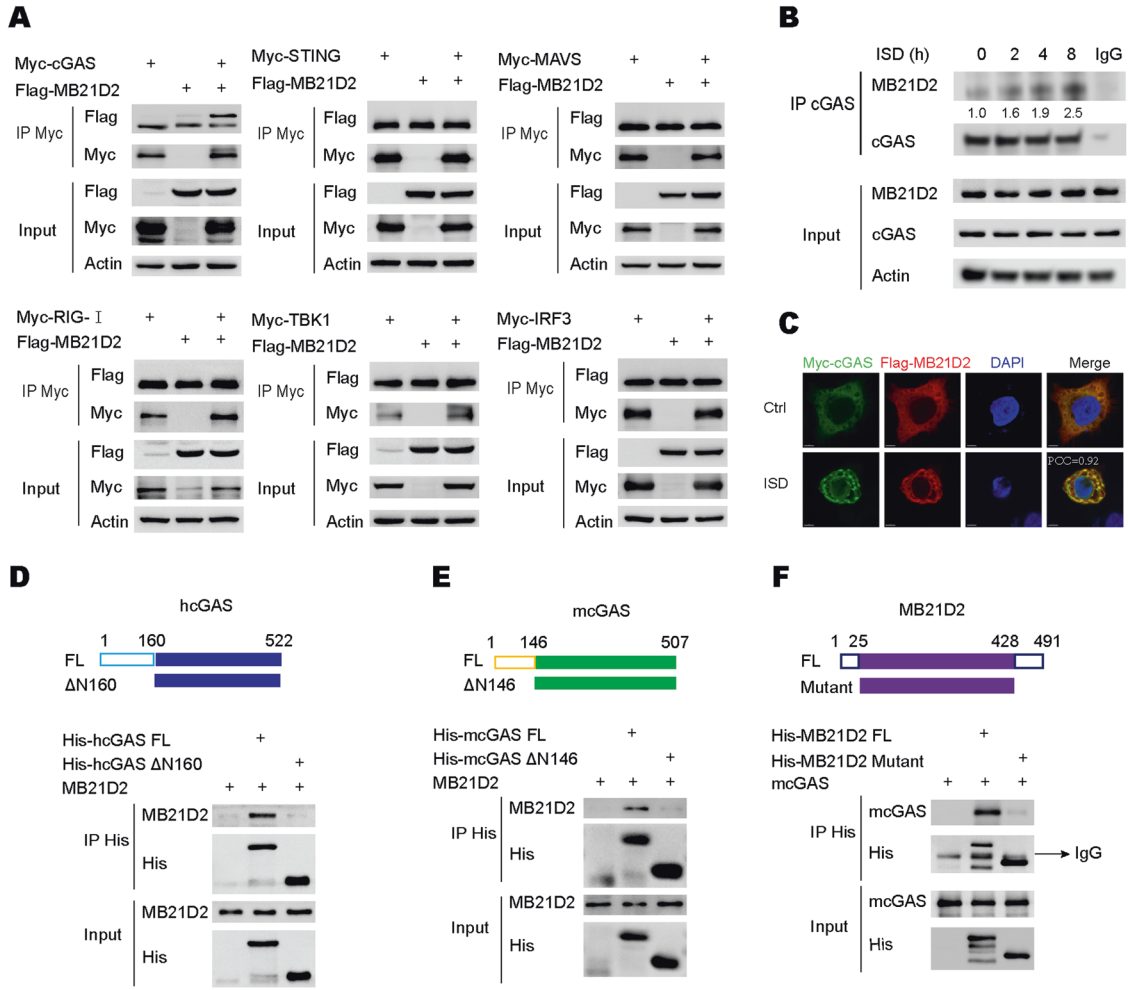

Fig. 3 MB21D2 interacted with cGAS. A HEK293T cells were respectively transfected with Myc-tagged cGAS, STING, RIG-I, MAVS, TBK1, or IRF3 together with Flag-tagged MB21D2 for 24 h. Coimmunoprecipitations and immunoblots were performed with indicated antibodies. **B** Coimmunoprecipitations and immunoblots of MB21D2 with cGAS in THP-1 cells after ISD stimulation for indicated times. **C** Microscopy images of cGAS and MB21D2 colocalization in HeLa cells. Pearson correlation coefficient (PCC) was analyzed by Image J. Scale bar, 5 μm. **D** Coimmunoprecipitations and immunoblots of purified His-tagged hcGAS FL or hcGAS-ΔN Mutant protein with purified MB21D2 protein. **E** Coimmunoprecipitations and immunoblots of purified His-tagged mcGAS FL or mcGAS-ΔN Mutant protein with purified MB21D2 protein. **F** Coimmunoprecipitations and immunoblots of purified His-tagged MB21D2 FL or MB21D2 Mutant protein with purified mcGAS protein.

MB21D2 promotes the enzymatic activity of cGAS

Binding of DNA to cGAS leads to the activation of cGAS and the production of cGAMP. To investigate whether MB21D2 promotes cGAS enzymatic activity, we first performed an in vitro cGAMP synthesis assay by using mcGAS protein in the presence or absence of MB21D2. The results showed that recombinant mcGAS could induce the production of cGAMP, while recombinant MB21D2 could not (Fig. 5A). Interestingly, we found cGAMP, produced by cGAS, was increased in the presence of recombinant MB21D2 (Fig. 5A, B). More importantly, we found MB21D2 promoted the cGAMP synthesis activity of mcGAS WT, but not its catalytic inactive form mcGAS (D213N) (Fig. 5A), which excluded the possibility that interaction of MB21D2 and cGAS triggers the activation of MB21D2. Moreover, we found MB21D2 robustly promoted the cGAS-mediated cGAMP production in a dose-dependent manner (Fig. 5C). However, MB21D2 deletion Mutant that could not bind to cGAS had no effect (Fig. 5C). We also measured the amount of cGAMP in mice macrophages prepared from WT and MB21D2 deficient mice upon ISD stimulation or HSV-1 infection. The production of cGAMP was greatly decreased in *Mb21d2*$^{-/-}$ mice macrophages compared to that in its counterparts (Fig. 5D). Similarly, we found the production of cGAMP was decreased in MB21D2 knockdown THP-1 cells upon ISD stimulation, or HSV-1 infection (Fig. 5E). The production of cGAMP upon ISD stimulation, or HSV-1 infection in *Mb21d2*$^{-/-}$ MEFs was also greatly decreased compared to that in its counterparts (Fig. 5F). Reintroduction of MB21D2 into *Mb21d2*$^{-/-}$ MEFs restored the ISD- or HSV-1-induced cGAMP production (Fig. 5F). Collectively, these data suggested that MB21D2 promotes the cGAS enzymatic activity to synthesize cGAMP.

MB21D2 promotes the liquid phase condensation of cGAS

cGAS contains a flexible N-terminal and a conserved C terminal, which containing the NTase domain. The N-terminal region is essential for the liquid phase condensation and DNA-binding of cGAS and cGAS enzymatic activity [10, 22]. To test whether binding of MB21D2 to the N-terminal of cGAS regulates its liquid phase condensation, we incubated fluorescently labeled hcGAS with double strand DNA in the presence or absence of MB21D2. Upon mixing, we found hcGAS and DNA mixture formed liquid droplets within 2 min as reported [10] (Fig. 6A). Interestingly, we found addition of MB21D2 (with a ration 1:1 to cGAS) to the cGAS and dsDNA mixture showed increased fluorescence intensity, especially at early time points, and larger equivalent diameter of the liquid droplets (Fig. 6A–C). However, MB21D2 alone could not

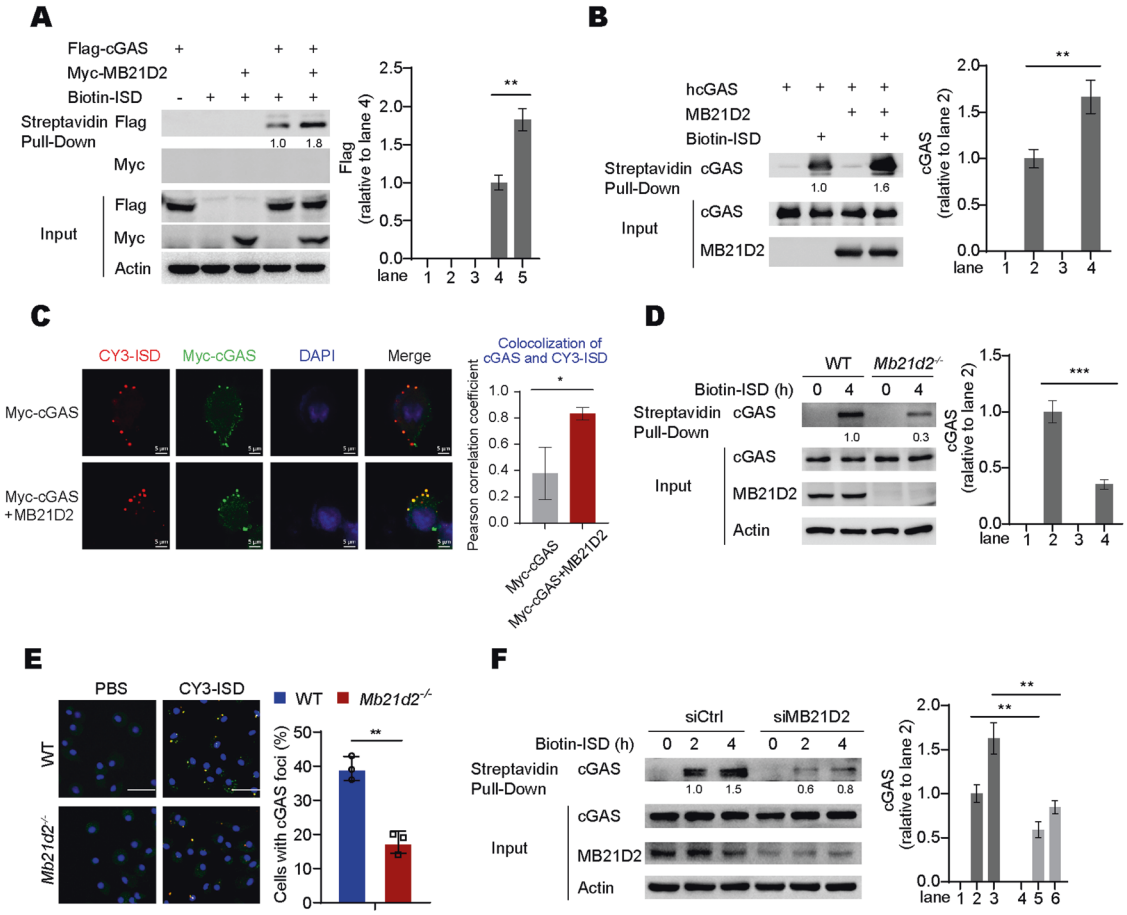

Fig. 4 MB21D2 promotes the DNA-binding affinity of cGAS. A HEK293T cells were overexpressed with Flag-cGAS and Myc-MB21D2 for 24 h, followed by Biotin-ISD stimulation for 4 h. The DNA-binding capacity of cGAS was analyzed by Streptavidin Pull-Down assay. Densitometric quantification was measured by Image J. **B** The DNA-binding capacity of purified hcGAS protein in the presence or absence of purified MB21D2 protein was analyzed by Streptavidin Pull-Down assay. Densitometric quantification was measured by Image J. **C** Microscopy images of cGAS-ISD puncta formation in the presence or absence of MB21D2 in HeLa cells. Pearson correlation coefficient was measured by Image J. Scale bar, 5 μm. **D** The DNA-binding capacity of cGAS in WT or *Mb21d2*$^{-/-}$ peritoneal macrophage cells was analyzed by Streptavidin Pull-Down assay. Densitometric quantification was measured by Image J. **E** Microscopy images of cGAS-ISD puncta formation in WT or *Mb21d2*$^{-/-}$ peritoneal macrophage cells (left). The percentage of cells with cGAS foci was quantified (right), at least 100 cells from each group were analyzed, $n = 3$. Scale bar, 30 μm. **F** THP-1 cells were transfected with control siRNA or MB21D2 siRNA for 48 h, followed by stimulated with Biotin-ISD for indicated times. The DNA-binding capacity of cGAS was analyzed by Streptavidin Pull-Down assay. Densitometric quantification was measured by Image J. Data are shown as mean ± SD and were analyzed by unpaired two-tailed Student's *t* test (**A**–**F**) (*$p < 0.05$, **$p < 0.01$, ***$p < 0.001$).

form liquid droplet with ISD even the concentration of both reached to 10 μM (Supplementary Fig. S6A). Moreover, we found MB21D2 deletion Mutant (residues 26–428) could not promote the liquid phase condensation of hcGAS when the concentration reached to 10 μM (Supplementary Fig. S6B), indicating that binding with MB21D2 is essential for the liquid phase condensation of hcGAS. We also observed that cGAS-DNA phase separation was robust and occurred at the concentration of ~50 nM of cGAS and ~30 nM of ISD in physiological buffer (Fig. 6D). More importantly, addition of MB21D2 lowered both the concentration of hcGAS and ISD to ~10 nM to form cGAS-DNA liquid droplets (Fig. 6D). As reported, long DNA has more binding sites for cGAS and is easier to drive cGAS droplets formation than shorter DNA [10]. We found 10 bp dsDNA can form droplets with hcGAS, when the concentration of hcGAS and DNA reached to 10 μM (Fig. 6E, Supplementary Fig. S6C), while addition of MB21D2 lowered the DNA length to 5 bp at the same condition (Fig. 6E, Supplementary Fig. S6C). Moreover, we showed that MB21D2 promoted the liquid phase condensation of hcGAS with various length of DNA (Supplementary Fig. S6D).

We next examined the formation of cGAS foci within cells. We first transfected Myc-cGAS into HeLa cells followed by infection with HSV-1. As reported [10], we found HSV-1 infection could promote the formation of cGAS foci in HeLa cells (Fig. 6F). Consistent with the promotion of cGAS droplet formation in vitro by MB21D2, we found more and larger cGAS granules were formed in HeLa cells with Flag-MB21D2 overexpression upon HSV-1 infection (Fig. 6F). Then we measured the dynamic liquid-like properties of these granules. We transfected GFP-cGAS into sg Ctrl and *MB21D2* sg KO HeLa cells for 24 h, and then transfected cells with CY3-ISD. We found cGAS formed puncta with ISD in the cytoplasm and these puncta exhibited dynamic internal rearrangement (Fig. 6G). Interestingly, we found cGAS-DNA foci were smaller in sg KO HeLa cells than its counterparts (Fig. 6G). These data demonstrated that MB21D2 promoted the phase separation of cGAS in vitro and in cells.

MB21D2 positively regulates antiviral response against DNA virus infection

IFNs play critical roles in antiviral immune responses [23]. To investigate the function of MB21D2 in cGAS-mediated antiviral

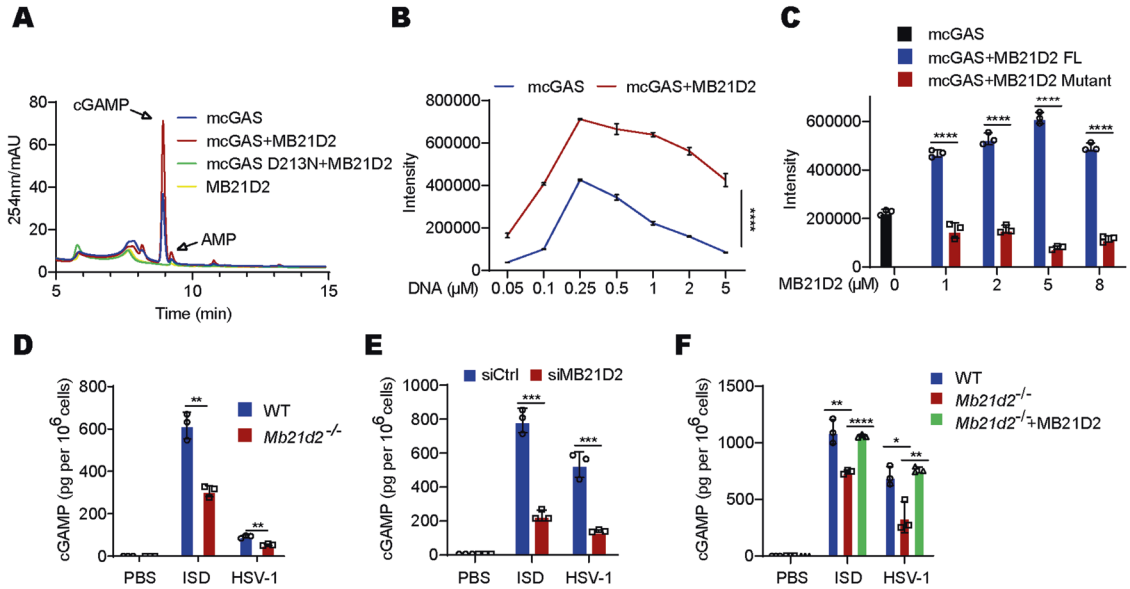

Fig. 5 MB21D2 promotes the enzymatic activity of cGAS. A Purified mcGAS, mcGAS D213N, and MB21D2 protein were incubated with 55 bp dsDNA. The production of cGAMP was analyzed by LC-MS. **B** Purified mcGAS protein, in the presence or absence of MB21D2 protein was incubated with indicated concentration of 55 bp dsDNA. The production of cGAMP was analyzed by LC-MS, $n = 3$. **C** Purified mcGAS protein, in the presence of indicated concentration of MB21D2 FL or MB21D2 Mutant protein was incubated with 55 bp dsDNA. The production of cGAMP was analyzed by LC-MS, $n = 3$. **D** WT or *Mb21d2*$^{-/-}$ peritoneal macrophages were stimulated with ISD, or infected with HSV-1 for 12 h. The production of cGAMP was analyzed by ELISA, $n = 3$. **E** ELISA quantification of cGAMP level in THP-1 cells transfected with control siRNA or MB21D2 siRNA for 48 h, followed by stimulated with ISD, or infected with HSV-1 for 12 h. **F** WT, *Mb21d2*$^{-/-}$ or *Mb21d2*$^{-/-}$ reintroduced of MB21D2 MEFs were stimulated with ISD, or infected with HSV-1 for 12 h. The production of cGAMP was analyzed by ELISA, $n = 3$. Data are shown as mean ± SD and were analyzed by unpaired two-tailed Student's *t* test (**B**–**F**) (*$p < 0.05$, **$p < 0.01$, ***$p < 0.001$, ****$p < 0.0001$).

immune responses, we isolated macrophages from WT and *Mb21d2*$^{-/-}$ mice and infected them with HSV-1. We found the genomic DNA copy number and the viral titers of HSV-1 were significant higher in *Mb21d2*$^{-/-}$ macrophages than its counterparts (Supplementary Fig. S7A). To investigate whether MB21D2-mediated antiviral function depends on cGAS, we transfected MB21D2 siRNA into *cgas*$^{-/-}$ macrophage to knockdown MB21D2 expression. The mRNA expression of *Ifnb1* in *cgas*$^{-/-}$ macrophages was greatly decreased. Similarly, we found the HSV-1 titers were higher in *cgas*$^{-/-}$ macrophages (Supplementary Fig. S7C). These data confirmed the essential role of cGAS in the regulation of HSV-1 infection. However, there was no significant change of *Ifnb1* mRNA expression and HSV-1 replication between *cgas*$^{-/-}$ and *cgas*$^{-/-}$+siMB21D2 macrophages (Supplementary Fig. S7C), which certified that MB21D2 regulates antiviral responses through cGAS. To investigate whether MB21D2 plays a role against RNA virus infection, we infected WT and *Mb21d2*$^{-/-}$ mice macrophages with VSV. Our results showed that the expression and secretion of IFN-β were not affected by MB21D2 deficiency upon VSV infection (Supplementary Fig. S7D, E). There was no significant difference between WT and *Mb21d2*$^{-/-}$ macrophages in the expression of *Ccl5* and *Cxcl10* upon VSV infection (Supplementary Fig. S7D). Consistently, we found that the expression of *VSV* mRNA, the VSV titers and the VSV G protein level were similar in WT and *Mb21d2*$^{-/-}$ macrophages upon VSV infection (Supplementary Fig. S7F-H).

Further, we measured the effect of MB21D2 on antiviral response in vivo. We found that *Mb21d2*$^{-/-}$ mice showed higher mortality than WT mice upon HSV-1 infection (Fig. 7A). The secretion level of IFN-β was much lower in the serum of *Mb21d2*$^{-/-}$ mice than that in WT mice (Fig. 7B). Consistently, we found the genomic DNA copy number and the viral titers of HSV-1 were significant higher in the brains of *Mb21d2*$^{-/-}$ mice than those in its counterparts (Fig. 7C). Moreover, the phosphorylation of STING, TBK1 and IRF3 in the brains of *Mb21d2*$^{-/-}$ mice was significant lower than WT mice (Supplementary Fig. S7B). Immunohistochemistry results indicated that *Mb21d2*$^{-/-}$ mice had more HSV-1 virions in the brains than WT mice (Fig. 7D).

To determine the cell types involved in the regulation of MB21D2 in antiviral immunity, we performed bone marrow transplantation (BMT) to generate bone marrow chimeric mice. We transplanted bone marrow cells of *Mb21d2*$^{-/-}$ mice or WT mice to lethally irradiated WT mice for 6 weeks, followed by infected with HSV-1. We found that the expression of *Ifnb1* in the brains of WT/BMT-*Mb21d2*$^{-/-}$ mice (transplantation of *Mb21d2*$^{-/-}$ bone marrow to irradiated WT mice) was significant lower than WT/BMT-WT mice (transplantation of WT bone marrow to irradiated WT mice) (Fig. 7E). The gDNA copy number and viral titers of HSV-1 in the brains were higher in WT/BMT-*Mb21d2*$^{-/-}$ mice, compared with those in WT/BMT-WT mice (Fig. 7F). Severe injuries and more infiltration of monocytes were observed in the lungs of WT/BMT-*Mb21d2*$^{-/-}$ mice after infection with HSV-1, relative to that in the lungs of WT/BMT-WT mice (Fig. 7G). Immunohistochemistry results showed that WT/BMT-*Mb21d2*$^{-/-}$ mice had more HSV-1 virions in the brains than WT/BMT-WT mice after HSV-1 injection (Fig. 7H). Together, these data indicated that MB21D2 in the cells of hematopoietic origin positively regulates cGAS-mediated antiviral response.

MB21D2 promotes antitumor immunity

Besides the important role in antiviral response, cGAS-STING pathway is also involved in antitumor immunity. Upon sensing the tumor released DNA, cGAS in DCs produces cGAMP. cGAMP in turn activates STING and then promotes the production of IFN-β, which leads to the CD8$^+$ T cells migration to the tumor [24] and initiates spontaneous natural antitumor T cell response [25]. To investigate whether MB21D2 is involved in antitumor immunity, we implanted B16-Luc cells into mice. We found the tumor grew faster in *MB21d2*$^{-/-}$ mice, compared to its counterparts (Fig. 8A, B, and Supplementary Fig. S8A, B). At the same time, we found the tumor growth was accelerated in WT/BMT-*MB21d2*$^{-/-}$ mice, compared to WT/BMT-WT mice (Fig. 8A, B). To investigate whether the faster growth of tumor in *MB21d2*$^{-/-}$ mice is due to lower cGAMP production, we injected cGAMP into *MB21d2*$^{-/-}$ mice. We

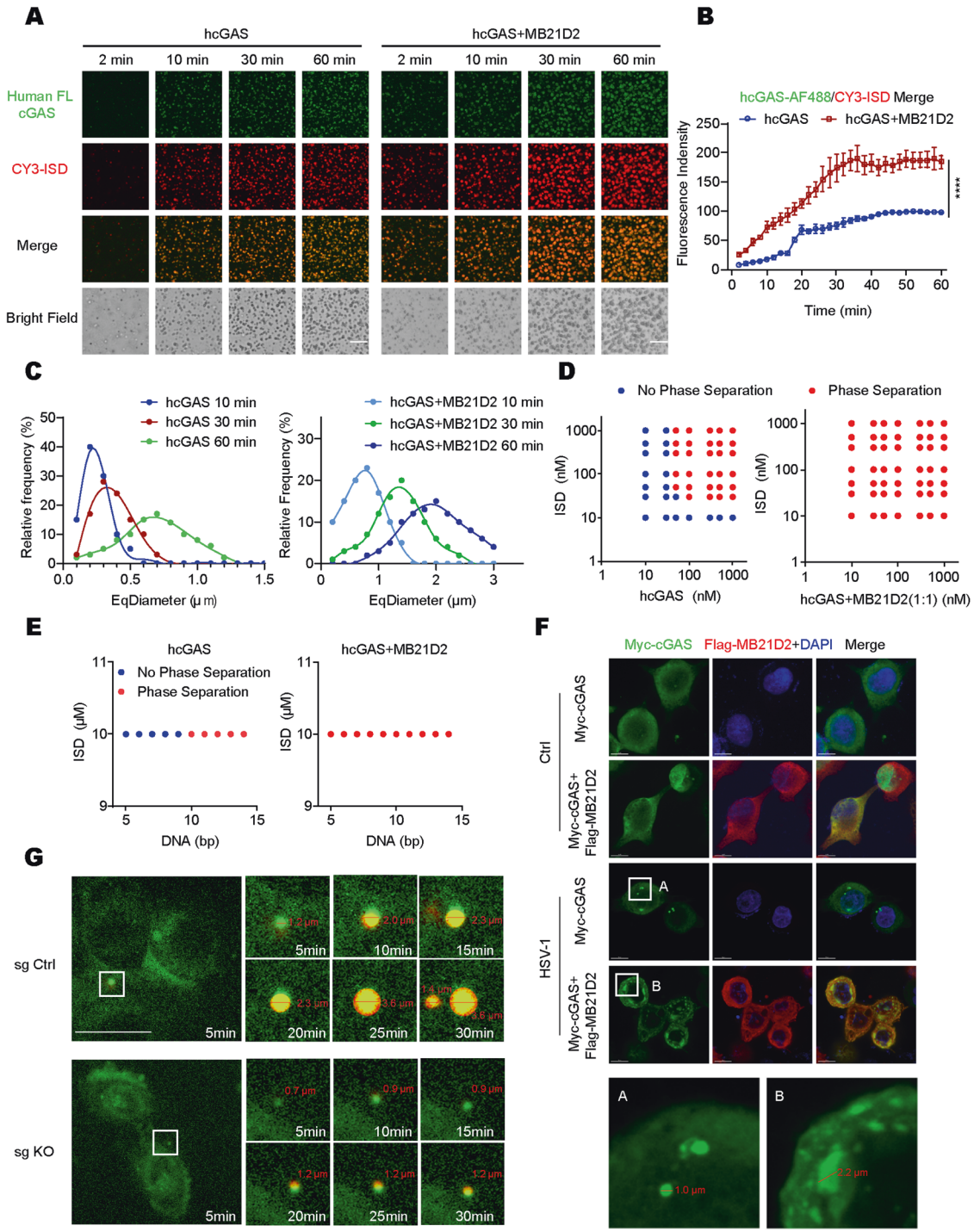

Fig. 6 MB21D2 promotes the liquid phase condensation of cGAS. A Time-lapse images of hcGAS-DNA phase separation in the presence or absence of MB21D2 (1:1 with hcGAS FL). Liquid droplets formed after mixing of 10 μM hcGAS FL (labeled with Alexa 488) with 10 μM CY3-ISD over 60 min. The images shown are representative of all fields in the well. Scale bar, 10 μm. **B** Fluorescence intensities of hcGAS-DNA liquid droplets in (**A**) over the time course of 60 min. Data were normalized to 100% by maximal fluorescence intensity in the absence of MB21D2, $n = 3$. **C** The diameter of the cGAS-DNA liquid droplets formed in (**A**) at the indicated time points, $n = 3$. **D** Phase separation diagram of hcGAS FL and ISD in the presence or absence of MB21D2 at the indicated concentrations. **E** Phase separation diagram of 10 μM hcGAS FL and 10 μM indicated length DNA in the presence or absence of 10 μM MB21D2. **F** Microscopy images of cGAS puncta formation after HSV-1 stimulation in HeLa cells. Scale bar, 10 μm. **G** Time-lapse images of cGAS (green) and CY3-ISD (red) puncta formation and fusion. Arrows indicate puncta. Scale bar, 10 μm. Data are shown as mean ± SD and were analyzed by unpaired two-tailed Student's *t* test (**B**) (****$p < 0.0001$).

found administration with cGAMP could decelerate the tumor growth (Supplementary Fig. S8A, B). The tumor-infiltrating $CD8^+$ T cells were significantly reduced in tumors of *MB21d2*$^{-/-}$ mice, compared with WT mice (Fig. 8C). Similarly, we showed less tumor-infiltrating $CD8^+$ T cells in tumors of WT/BMT-*MB21d2*$^{-/-}$ mice, compared with WT/BMT-WT mice (Fig. 8C). To explore the function of tumor-infiltrating $CD8^+$ T cells, we detected the protein levels of $CD8^+$ T cells' functional markers by flow cytometry. Much

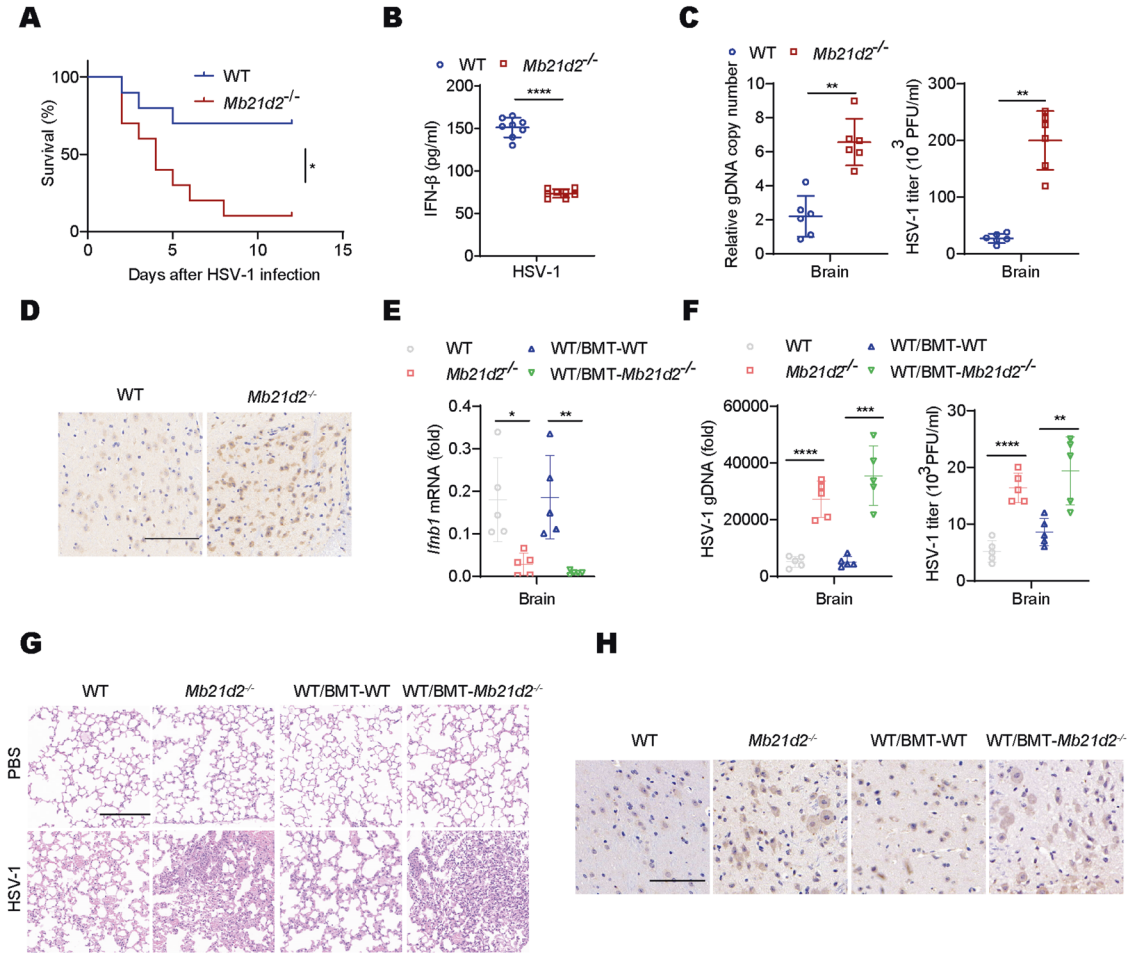

Fig. 7 MB21D2 positively regulates anti-DNA viral infection. A Survival of WT or *Mb21d2*$^{-/-}$ mice ($n = 10$ per group) after intravenous injection of HSV-1 (3×10^7 PFU per mouse). **B** IFN-β production in serum from WT or *Mb21d2*$^{-/-}$ mice 8 h after intravenous injection of HSV-1 (1×10^7 PFU per mouse) ($n = 8$ per group). **C** HSV-1 genomic DNA copy number and HSV-1 titers in the brains of WT or *Mb21d2*$^{-/-}$ mice 3 d after intravenous injection of HSV-1 (1×10^7 PFU per mouse) ($n = 6$ per group). **D** Immunohistochemistry of HSV-1 in the brains of WT or *Mb21d2*$^{-/-}$ mice 3 d after intravenous injection of HSV-1 (1×10^7 PFU per mouse). Scale bar, 150 μm. **E** RT-PCR analysis of *Ifnb1* in the brains of WT, *Mb21d2*$^{-/-}$, WT/BMT-WT or WT/BMT-*Mb21d2*$^{-/-}$ mice 3 d after intravenous injection of HSV-1 (1×10^7 PFU per mouse) ($n = 5$ per group). **F** HSV-1 genomic DNA copy number and HSV-1 titers in the brains of WT, *Mb21d2*$^{-/-}$, WT/BMT-WT or WT/BMT-*Mb21d2*$^{-/-}$ mice treated as in (**E**). **G** Hematoxylin-eosin staining of lung sections from mice as in (**E**). Scale bars, 200 μm. **H** Immunohistochemistry of HSV-1 in the brains from mice as in (**E**). Scale bar, 100 μm. Data are shown as mean ± SD and were analyzed by unpaired two-tailed Student's *t* test (**B**, **C**, **E** and **F**). In the mouse survival study, Kaplan–Meier survival curves were generated and analyzed for statistical significance (**A**) (*$p < 0.05$, **$p < 0.01$, ***$p < 0.001$, ****$p < 0.0001$).

reduced IFN-γ-, granzyme B- and perforin-producing CD8$^+$ T cells were found in tumors from *MB21d2*$^{-/-}$ mice, compared to WT mice (Fig. 8D). The percentage of IFN-γ-, granzyme B- and perforin-producing CD8$^+$ T cells was also lower in WT/BMT-*MB21d2*$^{-/-}$ mice than WT/BMT-WT mice (Fig. 8D), suggesting that MB21D2 promotes the generation of cytotoxic CD8$^+$ T cells that infiltrate tumors. Then, we measured the percentage of memory and activated T cells in mice tumors. We found CD62L$^-$CD8$^+$ and CD69$^+$CD8$^+$ T cells were decreased in *MB21d2*$^{-/-}$ mice tumors than those counterparts (Fig. 8E). Consistently, much less CD62L$^-$CD8$^+$ and CD69$^+$CD8$^+$ T cells were found in tumors of WT/BMT-*MB21d2*$^{-/-}$ mice, compared to WT/BMT-WT mice (Fig. 8E), which indicated that MB21D2 enhanced memory and activated T-cell proportion.

As reported, IFNs can induce the phenotypic maturation of DCs by enhancing the expression of MHC I, MHC II and costimulatory molecules (such as CD40, CD80 and CD86) [26, 27] and initiate a specific T cell response. Here, we found that the mean fluorescent intensity of CD80, CD86 and MHC II was lower in *MB21d2*$^{-/-}$ mice tumor-draining lymph node (TDLN) DCs than WT mice TDLN DCs (Fig. 8F). Consistently, we showed that DCs from TDLN isolated from WT/BMT-*MB21d2*$^{-/-}$ mice displayed much decreased maturation and reduced capability in antigen presentation than WT/BMT-WT mice (Fig. 8F). Taken together, these data suggested that MB21D2 is required for cGAS-mediated antitumor immunity.

DISCUSSION

In this study, we revealed a critical role of MB21D2 in regulating cGAS-mediated IFNs signaling. We found that MB21D2 directly bound to cGAS N-terminal, facilitated the liquid phase condensation, DNA-binding efficiency, and enzymatic activation of cGAS upon ISD stimulation, or HSV-1 infection. MB21D2 deficiency dramatically decreased cGAS-mediated IFNs production in THP-1 cells and mice macrophages. Consistently, *Mb21d2*$^{-/-}$ mice were more susceptible to DNA virus HSV-1 infection, compared to wild-type mice. However, there were no significant differences in the expression of *Ifnb1* and virus replication between WT and *Mb21d2*$^{-/-}$ mice macrophages upon RNA virus VSV infection. More importantly, MB21D2 also plays a positive role in antitumor effect.

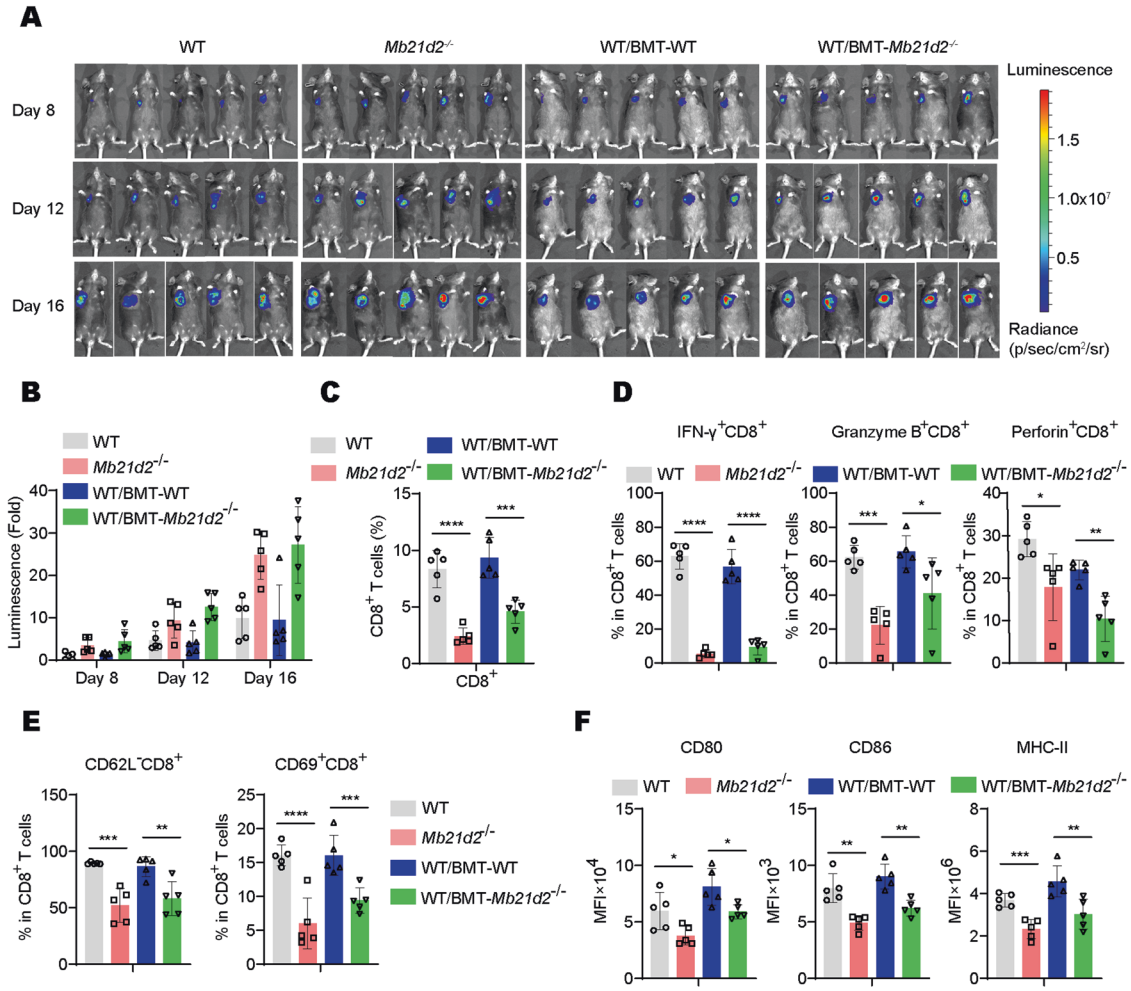

Fig. 8 MB21D2 positively regulates antitumor immunity. A Representative bioluminescent images of tumors are shown for WT, *Mb21d2*$^{-/-}$, WT/BMT-WT or WT/BMT-*Mb21d2*$^{-/-}$ mice implanted with B16-Luc cells, $n = 5$. **B** Bioluminescent quantification of tumors in WT, *Mb21d2*$^{-/-}$, WT/BMT-WT or WT/BMT-*Mb21d2*$^{-/-}$ mice implanted with B16-Luc cells for indicated times, $n = 5$. **C** The percentage of CD8$^+$ T cells in tumors from WT, *Mb21d2*$^{-/-}$, WT/BMT-WT or WT/BMT-*Mb21d2*$^{-/-}$ mice 17 d after B16-Luc cells implanted, $n = 5$. **D** The percentage of IFN-γ$^+$CD8$^+$ T cells, Granzyme B$^+$CD8$^+$ T cells and Perforin$^+$CD8$^+$ T cells in tumors from mice as in (**C**), $n = 5$. **E** The percentage of CD62L$^-$CD8$^+$ T cells and CD69$^+$CD8$^+$ T cells in tumors from mice as in (**C**), $n = 5$. **F** Mean fluorescent intensity (MFI) of CD80, CD86 and MHC II in tumor-draining lymph node DCs from mice as in (**C**), $n = 5$. Data are shown as mean ± SD and were analyzed by unpaired two-tailed Student's *t* test (**C**–**F**) (*$p < 0.05$, **$p < 0.01$, ***$p < 0.001$, ****$p < 0.0001$).

Mb21d2$^{-/-}$ mice showed enhanced tumor growth, with decreased tumor-infiltrating CD8$^+$ T cells.

MB21D2 belongs to the CD-NTase family and its function is not well defined. MB21D2 is predicated to have a complete active site and probably capable of catalytic function [16]. In this study, we found that MB21D2 alone could not bind to DNA, while MB21D2 was needed for promoting efficient DNA sensing of cGAS. Upon binding to DNA, cGAS forms homodimers, oligomers and further liquid-like droplets, which are critical for cGAMP formation. Our data showed that the liquid phase condensation was undetectable when we mixed MB21D2 alone with DNA and there was no MB21D2-CY3-ISD foci in the cytoplasm of HeLa cells. However, MB21D2 promoted the formation of cGAS-DNA droplets both in vitro and in cells. More importantly, in vitro cGAMP synthesis assay showed that MB21D2 alone could not catalyze the formation of cGAMP, while MB21D2 facilitated the enzymatic activation of cGAS for producing cGAMP.

cGAS is an important DNA sensor for efficient innate immune response to cytosolic dsDNA and DNA virus. Aberrant activation of immune response leads to several severe autoimmune diseases [28–30]. Thus, precise regulation of cGAS activity is absolutely necessary. Previous studies showed that PCBP1 [31], IFI16 [32], and G3BP1 [33] all can promote the DNA recognition of viral DNA by cGAS. Another study showed that OASL directly binds to cGAS independently of DNA and inhibits cGAS activation during DNA virus infection [19]. In this study, we identified that MB21D2 functions as a positive regulator of cGAS activity in modulating the antiviral immune response upon DNA virus infection. MB21D2 deficiency led to dramatically decreased IFN-β signaling and increased virus replication. Although cGAS is also reported to plays an important role in RNA virus infection [34, 35]. However, our results indicated that MB21D2 had no effect on RNA virus-induced IFN-β signaling.

Besides the function on antiviral immune response, cGAS is also essential for cellular senescence [36] and antitumor immunity [37, 38]. A recent report showed that MB21D2 is overexpressed in various cancer types, and its Q311E Mutant appears in four human squamous cell carcinomas (SCCs) [39]. A kind of DNA virus HPV is a major risk factor for head and neck squamous cell carcinoma (HNSCC). The report showed that MB21D2 overexpression was correlated negatively with HPV infection, which is high consistent with our findings. Besides, our findings showed that MB21D2

positively regulated anti-melanoma through targeting cGAS. MB21D2 promoted TDLN DCs maturation and tumor-specific antigen presentation, augmented $CD8^+$ T cell differentiation and activation. *Mb21d2*$^{-/-}$ mice showed faster tumor growth and less $CD8^+$ T cells infiltration within the tumors, compared to WT mice.

In summary, we found that MB21D2 was critically involved in the host antiviral and antitumor through mediated cGAS-DNA liquid droplets formation to trigger IFN response. MB21D2 acted as an important activator of cGAS which may provide some therapeutic clues for drug design and vaccine development to immunodeficiency disease and cancer.

MATERIALS AND METHODS

Mice

Mb21d2$^{-/-}$ mice were purchased from Cyagen Biosciences. Primers used for mice genotyping were as follows: forward 1: 5′-TGTCATTGTTAGCAGGATGTGTGC-3′, forward 2: 5′-AAGAAGACTATGCAGCCCACTTT-3′, reverse: 5′-ATAATACTGT TTCAGAGCCCGCA-3′. Chimeric mice were generated using bone marrow transplantation as previously described [40]. All mouse experiments were performed following the general guidelines published by the Association for Assessment and Accreditation of Laboratory Animal Care. All mice were on the C57BL/6 background and were maintained under specific-pathogen free conditions with the approval of the Scientific Investigation Board of the Medical School of Shandong University.

Cell culture

HEK293T cells, HeLa cells, mice macrophages and MEFs were cultured at 37 °C under 5% CO_2 in DMEM supplemented with 10% fetal bovine serum (FBS), 100 U/ml penicillin and 100 μg/ml streptomycin. THP-1 cells and B16-luc melanoma cells were cultured at 37 °C under 5% CO_2 in RPMI 1640 medium supplemented with 10% FBS, 100 U/ml penicillin and 100 μg/ml streptomycin. For transfection of plasmids into HEK293T cells and HeLa cells, Lipofectamine 2000 (Invitrogen) or Lipofectamine 3000 (Invitrogen) was used. For transfection of plasmids into MEFs, jetOPTIMUS (polyplus) was used according to the manufacturer's instruction. For transfection of siRNA into THP-1 cells, Lipofectamine RNAiMAX (Invitrogen) was used according to the manufacturer's instruction. All siRNAs were obtained from Genepharma (Supplementary Table S2). To make MB21D2 KO cells, we transfected recombinant lentiCRISPR v2 plasmid, which contains ds-oligonucleotides targeting *Mb21d2* into HeLa cells. Transduced cells were selected with puromycin (1 μg/ml) for 2 d. The knockout efficiency was confirmed by DNA sequencing.

Viruses

Macrophages were infected with VSV (0.1 MOI), or HSV-1 (10 MOI) for indicated time. The plaque assay of HSV-1 or VSV was performed on Vero cells. For in vivo experiments, age- and sex-matched WT and *Mb21d2*$^{-/-}$ mice were intravenous infected with HSV-1 (3×10^7 PFU per mouse).

Antibodies and reagents

The following antibodies were used: anti-cGAS (#31659), anti-cGAS (#83623), anti-TBK1 (#3013), anti-phospho-TBK1 (#5483), anti-IRF3 (#4302), anti- phospho-IRF3 (#4947), anti-Myc (#2276) were purchased from Cell Signaling Technology; anti-VSV-G (V5507), anti-MB21D2 (SAB2108874) were purchased from Sigma-Aldrich; anti-Flag (PA1-984B) was purchased from Thermo Fisher Scientific; anti-HA (sc-7392), anti-Actin (sc-58673) were purchased from Santa Cruz Biotechnology; FITC anti-mouse CD3 (#100203), PE anti-mouse IFN-γ (#505807), APC anti-mouse Perforin (#154403), PE/Cy7-anti-mouse CD80 (#104733), PerpCP/Cyanine5.5 anti-mouse CD86 (#105027), FITC anti-mouse CD11c (#117305) were purchased from BioLegend; PE anti-mouse CD62L (#561918), PerCP-Cy5.5 anti-mouse CD8α (#561109), APC anti-mouse CD69 (#560689), PE/Cyanine7 anti-human/mouse Granzyme B (#372213) were purchased from BD Biosciences; APC anti-mouse-MHC class II (ab93559) was purchased from Abcam. All antibodies were used according to the manufacturer's instructions. 2′, 3′-cGAMP was purchased from InvivoGen. For Biotin Pull-Down assay, Streptavidin-Agarose (S1638, Sigma-Aldrich) was used.

Plasmids

The cDNA fragments encoding human CD-NTase family members were amplified from THP-1 cells and cloned into pCMV-N-Myc plasmid, respectively. The cDNA encoding mouse MB21D2 were amplified from mice macrophages and cloned into pFLAG-CMV-2 plasmid. For MB21D2 deletion, a gRNA (ATACGACGACCAGAGAGCGC) targeting human MB21D2 was cloned into lentiCRISPR v2 plasmid [41]. For *Escherichia coli* expression, cDNA of human cGAS (hcGAS), hcGAS (ΔN160, 161–522), mouse cGAS (mcGAS), mcGAS (ΔN146, 147–507), mouse MB21D2 and MB21D2 Mutant (residues 26–428) were cloned into pET-28a (Novagen) plasmid to express SUMO fusion proteins (pET-28a-SUMO) between BamHI and XhoI sites, resulting in a plasmid encoding an N-terminal hexahistidine-SUMO tagged proteins. Mutant of mcGAS (D213N) was generated by QuikChange site-directed mutagenesis. Other plasmids used in this study were described previously [42]. All constructs were confirmed by DNA sequencing.

RT-qPCR

Cells were collected and total RNA was extracted by using RNA fast200 kit (Fastagen). The RNA was reverse-transcripted and analyzed by qPCR on a LightCycler (Bio-Rad). The primers were listed in Supplementary Table S1. The mRNA level of the genes was normalized to the expression of *β-actin*, and the $2^{-\Delta\Delta Ct}$ method was used to calculate relative expression changes.

ELISA

Mice serum or cell supernatants were collected and measured for the concentration of IFN-β by using a mouse IFN-β ELISA kit (BioLegend) according to the manufacturer's instruction.

Coimmunoprecipitation and immunoblot analysis

Whole-cell extracts were collected and lysed in IP buffer (1% NP-40, 50 mM Tris-HCl pH 7.4, 50 mM EDTA, 150 mM NaCl) supplemented with a protease inhibitor cocktail (sigma), followed by concentration at $14{,}000 \times g$ for 10 min. The supernatants were incubated with specific antibodies at 4 °C overnight, and then protein A/G plus–agarose was added. The immunoprecipitants were washed four to six times with IP buffer and boiled in 1 × SDS loading buffer (60 mM Tris-HCl pH 6.8, 1% SDS, 5% glycerol, 0.005% bromophenol blue and 1% 2-mercaptoethanol).

For immunoblot analysis, immunoprecipitates or whole-cell lysates were separated by SDS–PAGE, transferred onto nitrocellulose membranes and then blotted with specific antibodies. Proteins were visualized by enhanced chemiluminescence according to the manufacturer's instruction (Thermo Fisher Scientific). Original Western blots for all relevant Figures were shown in "Original Western blot Images".

Protein expression and purification

The gene sequence encoding full-length hcGAS or mcGAS were optimized and synthesized (Beijing AuGCT DNA-SYN Biotechnology Co., Ltd, China). Expression vectors were transformed into *E. coli* strain BL21-CodonPlus (DE3)-RIPL. Transformed strains were grown in LB medium containing kanamycin (50 mg/l) and chloramphenicol (25 mg/l) at 37 °C until an OD600 of approx 0.6. The temperature was then shifted to 18 °C and the strains were induced by the addition of 0.1 mM Isopropyl β-D-thiogalactoside (IPTG). After induction, the strains were grown overnight. The 6 × His-SUMO-tagged proteins (His-SUMO-hcGAS, His-SUMO-mcGAS and His-SUMO-MB21D2) were purified over a Ni-NTA affinity column, and then a heparin column, followed by gel filtration on a Superdex 200 10/300 GL column. The peak fractions of the proteins were pooled, flash-frozen in liquid nitrogen and stored at −80 °C for using further. As for the 6 × His-SUMO-tag-cleaved proteins, the purification procedure is the same as the tagged proteins, except one more step to remove the 6 × His-SUMO tag by using ULP1 cleavage before being loaded onto a heparin column. The truncation hcGAS ΔN160, mcGAS ΔN146, and Mutant (mcGAS D213N) were purified using the same protocol used for the FL protein respectively. The truncation MB21D2 Mutant was also purified using the same protocol used for the wild-type MB21D2 except not using heparin column.

Protein labeling

Purified human cGAS was labeled with Alexa Fluor 488 (Thermo Fisher Scientific) according to manufacturer's protocol.

In vitro phase separation assay and image collection

In general, recombinant cGAS protein (Alexa Fluor 488-labeled) was mixed with ISD (Cy3-labeled) in 18-well plates (ibidi) coated with 20 mg/ml BSA (Sigma). Mixtures were incubated and images were captured at indicated times. Phase separation of recombinant cGAS with ISD was performed in 20 mM Tris-HCl pH 7.5, 150 mM NaCl and 1 mg/ml BSA. Phase separation diagram was performed in a physiological buffer (20 mM Tris-HCl pH 7.5, 15 mM NaCl, 135 mM KCl, 5 mM phosphate, 1.5 mM $MgCl_2$, and 1 mg/ml BSA).

Phase-separated droplets were imaged by using Zeiss LSM780 confocal microscope with a 40 × oil objective. Time-lapse images of cGAS–DNA phase separation were captured every 2 min over 1 h. Fluorescence intensities and EqDiameter (the diameter of a circle with the same area as the measured object) of phase-separated droplets were quantified using ImageJ software. The distribution of droplets EqDiameter was plotted using GraphPad Prism 8.

Live-cell imaging

Cells were plated onto 35-mm glass bottom dishes to a proper density. Cells were transfected with GFP-cGAS for 48 h and then stimulated with CY3-ISD. Live-cell images were captured by using Andor Dragonfly (Andor) with a 40 × oil objective. Images were analyzed by ImarisViewer.

Determination of enzymatic activity of cGAS and MB21D2 in vitro

In vitro enzymatic activity was measured by monitoring the formation of the product 2′, 3′-cGAMP by using a HPLC system (SHIMADZU, LC-10A) equipped with LC-10AT pumps and an ultraviolet detector SPD-10AV. The initial reaction mixture contained one target protein (1 μM mcGAS, 1 μM mcGAS ΔN146, or 2 μM MB21D2), 25 mM Tris-HCl pH 8.0, 70 mM NaCl, 5 mM $MgCl_2$, 1 mM ATP, 1 mM GTP, 55 bp dsDNA at 1.2 μM. To further investigate the effect of MB21D2 on mcGAS activation, the reaction mixture contained 1 μM mcGAS or mcGAS ΔN146, 25 mM Tris-HCl pH 8.0, 70 mM NaCl, 5 mM $MgCl_2$, 1 mM ATP, 1 mM GTP, 55 bp dsDNA at 1.2 μM, and MB21D2 or MB21D2 Mutant with varying concentrations. Each reaction in 30 μl mixture was incubated at 25 °C for 10 min, and terminated by heated at 85 °C for 10 min, and centrifuged at 16,000 × g for 10 min. The supernatant was then analyzed by an YMC-pack pro-C18 reverse phase column (4.6 × 250 mm, 5 μm, YMC). Analytes were monitored by UV 254 nm. Phase A contained 5 mM ammonium acetate (pH 5.0) in water and phase B was 100% acetonitrile. The samples were eluted using a linear gradient from 2% B to 15% B at a flow rate of 1 ml/min over 15 min. The product 2′, 3′-cGAMP was quantified by measuring the peak area (unit, uAU·Sec) of 2′, 3′-cGAMP at the 254 nm. Each experiment was performed in triplicate.

cGAS enzymatic activity assay in cells

Macrophages, MEFs, or THP-1 cells were plated into 10 cm dishes, and cells were stimulated with ISD, or infected with HSV-1 for indicated times, and then cells were harvested and resuspended in RIPA Lysis and Extraction buffer (Thermo Fisher Scientific). The lysates were centrifuged at 14,000 × *g*, 4 °C for 10 min and the 2′, 3′-cGAMP level was measured by using a 2′, 3′-cGAMP ELISA kit (Cayman Chemical) according to the manufacturer's instruction.

Immunofluorescence staining and microscopy

Cells cultured on coverslips were fixed with 4% PFA for 10 min, and then permeabilized with 0.5% Triton X-100 for 10 min at room temperature. After incubation in blocking buffer (1 mg/ml BSA, 3% goat serum, 0.05% saponin, 1 mM EDTA in TBS) for 1 h, primary antibodies were added and incubated overnight at 4 °C. After 4 times washes with TBS and 0.05% saponin, samples were further stained with suitable Alexa Fluor 568- or Alexa Fluor 488-conjugated secondary antibodies (Thermo Fisher Scientific). Nuclei were stained with DAPI (4′, 6′-diamidino-2-phenylindole hydrochloride, Molecular Probes, Invitrogen). Images were acquired using confocal laser microscopy LSM780 (Carl Zeiss) or Andor Dragonfly (Andor).

Tumor models

B16-luc melanoma cells (1×10^6) were resuspended in 100 μl PBS and implanted s.c. into the right flank of WT or *Mb21d2*$^{-/-}$ mice. After 7 d, for tumor imaging in vivo, luciferin was injected i.p. and imaged using an IVIS Spectrum imaging system (PerkinElmer).

Statistical analysis

Statistical details for each experiment can be found in the figure legends, and outlined in the corresponding methods details section. A standard two-tailed unpaired Student's *t* test was used for statistical analysis of two groups. In the mouse survival study, Kaplan–Meier survival curves were generated and analyzed for statistical significance. Statistical analyzed data were expressed as mean ± SD. A p value < 0.05 is considered as statistically significant. The p values represented as $^*p < 0.05$, $^{**}p < 0.01$, $^{***}p < 0.001$, $^{****}p < 0.0001$. We performed the statistical analyses by using GraphPad Prism 8.

DATA AVAILABILITY

All data are available from the authors upon request.

REFERENCES

1. Wu J, Sun L, Chen X, Du F, Shi H, Chen C, et al. Cyclic GMP-AMP is an endogenous second messenger in innate immune signaling by cytosolic DNA. Science. 2013;339:826–30.
2. Li XD, Wu J, Gao D, Wang H, Sun L, Chen ZJ. Pivotal roles of cGAS-cGAMP signaling in antiviral defense and immune adjuvant effects. Science. 2013;341:1390–4.
3. Gao P, Ascano M, Wu Y, Barchet W, Gaffney BL, Zillinger T, et al. Cyclic [G(2′, 5′)pA(3′, 5′)p] is the metazoan second messenger produced by DNA-activated cyclic GMP-AMP synthase. Cell. 2013;153:1094–107.
4. Ablasser A, Goldeck M, Cavlar T, Deimling T, Witte G, Röhl I, et al. cGAS produces a 2′–5′-linked cyclic dinucleotide second messenger that activates STING. Nature. 2013;498:380–4.
5. Gao P, Ascano M, Zillinger T, Wang W, Dai P, Serganov AA, et al. Structure-function analysis of STING activation by c[G(2′, 5′)pA(3′, 5′)p] and targeting by antiviral DMXAA. Cell. 2013;154:748–62.
6. Medzhitov R. Recognition of microorganisms and activation of the immune response. Nature. 2007;449:819–26.
7. Diamond MS, Kinder M, Matsushita H, Mashayekhi M, Dunn GP, Archambault JM, et al. Type I interferon is selectively required by dendritic cells for immune rejection of tumors. J Exp Med. 2011;208:1989–2003.
8. Zhang X, Wu J, Du F, Xu H, Sun L, Chen Z, et al. The cytosolic DNA sensor cGAS forms an oligomeric complex with DNA and undergoes switch-like conformational changes in the activation loop. Cell Rep. 2014;6:421–30.
9. Li X, Shu C, Yi G, Chaton CT, Shelton CL, Diao J, et al. Cyclic GMP-AMP synthase is activated by double-stranded DNA-induced oligomerization. Immunity. 2013;39:1019–31.
10. Du M, Chen ZJ. DNA-induced liquid phase condensation of cGAS activates innate immune signaling. Science. 2018;361:704–9.
11. Zhou W, Mohr L, Maciejowski J, Kranzusch PJ. cGAS phase separation inhibits TREX1-mediated DNA degradation and enhances cytosolic DNA sensing. Mol Cell. 2021;81:739–55.e7.
12. Andreeva L, Hiller B, Kostrewa D, Lässig C, de Oliveira Mann CC, Jan, Drexler D, et al. cGAS senses long and HMGB/TFAM-bound U-turn DNA by forming protein-DNA ladders. Nature 2017;549:394–8.
13. Luecke S, Holleufer A, Christensen MH, Jønsson KL, Boni GA, Sørensen LK, et al. cGAS is activated by DNA in a length-dependent manner. EMBO Rep. 2017;18:1707–15.
14. Liu ZS, Cai H, Xue W, Wang M, Xia T, Li WJ, et al. G3BP1 promotes DNA binding and activation of cGAS. Nat Immunol. 2019;20:18–28.
15. Hu S, Sun H, Yin L, Li J, Mei S, Xu F, et al. PKR-dependent cytosolic cGAS foci are necessary for intracellular DNA sensing. Sci Signal. 2019;12:eaav7934.
16. Kranzusch PJ. cGAS and CD-NTase enzymes: structure, mechanism, and evolution. Curr Opin Struct Biol. 2019;59:178–87.
17. Schwartz SL, Conn GL. RNA regulation of the antiviral protein 2′-5′-oligoadenylate synthetase. Wiley Interdiscip Rev RNA. 2019;10:e1534.
18. Zhu J, Zhang Y, Ghosh A, Cuevas RA, Forero A, Dhar J, et al. Antiviral activity of human OASL protein is mediated by enhancing signaling of the RIG-I RNA sensor. Immunity. 2014;40:936–48.
19. Ghosh A, Shao L, Sampath P, Zhao B, Patel NV, Zhu J, et al. Oligoadenylate-synthetase-family protein OASL inhibits activity of the DNA sensor cGAS during DNA virus infection to limit interferon production. Immunity. 2019;50:51–63.e5.
20. Kranzusch PJ. cGAS and CD-NTase enzymes: structure, mechanism, and evolution. Curr Opin Struct Biol. 2019;59:178–87.
21. Song G, Liu B, Li Z, Wu H, Wang P, Zhao K, et al. E3 ubiquitin ligase RNF128 promotes innate antiviral immunity through K63-linked ubiquitination of TBK1. Nat Immunol. 2016;17:1342–51.

22. Tao J, Zhang XW, Jin J, Du XX, Lian T, Yang J, et al. Nonspecific DNA Binding of cGAS N Terminus Promotes cGAS Activation. J Immunol. 2017;198:3627–36.
23. van Boxel-Dezaire AH, Rani MR, Stark GR. Complex modulation of cell type-specific signaling in response to type I interferons. Immunity. 2006;25:361–72.
24. Corrales L, Matson V, Flood B, Spranger S, Gajewski TF. Innate immune signaling and regulation in cancer immunotherapy. Cell Res. 2017;27:96–108.
25. Woo SR, Fuertes MB, Corrales L, Spranger S, Furdyna MJ, Leung MY, et al. STING-dependent cytosolic DNA sensing mediates innate immune recognition of immunogenic tumors. Immunity. 2014;41:830–42.
26. Santini SM, Lapenta C, Logozzi M, Parlato S, Spada M, Di Pucchio T, et al. Type I interferon as a powerful adjuvant for monocyte-derived dendritic cell development and activity in vitro and in Hu-PBL-SCID mice. J Exp Med. 2000;191:1777–88.
27. Crouse J, Kalinke U, Oxenius A. Regulation of antiviral T cell responses by type I interferons. Nat Rev Immunol. 2015;15:231–42.
28. Baechler EC, Batliwalla FM, Karypis G, Gaffney PM, Ortmann WA, Espe KJ, et al. Interferon-inducible gene expression signature in peripheral blood cells of patients with severe lupus. Proc Natl Acad Sci USA. 2003;100:2610–5.
29. Crow YJ, Manel N. Aicardi-Goutières syndrome and the type I interferonopathies. Nat Rev Immunol. 2015;15:429–40.
30. Kiriakidou M, Ching CL. Systemic lupus erythematosus. Ann Intern Med. 2020;172:Itc81–itc96.
31. Liao CY, Lei CQ, Shu HB. PCBP1 modulates the innate immune response by facilitating the binding of cGAS to DNA. Cell Mol Immunol. 2021;18:2334–43.
32. Almine JF, O'Hare CA, Dunphy G, Haga IR, Naik RJ, Atrih A, et al. IFI16 and cGAS cooperate in the activation of STING during DNA sensing in human keratinocytes. Nat Commun. 2017;8:14392.
33. Dai J, Huang YJ, He X, Zhao M, Wang X, Liu ZS, et al. Acetylation blocks cGAS activity and inhibits self-DNA-induced autoimmunity. Cell. 2019;176:1447–60.e14.
34. Schoggins JW, MacDuff DA, Imanaka N, Gainey MD, Shrestha B, Eitson JL, et al. Pan-viral specificity of IFN-induced genes reveals new roles for cGAS in innate immunity. Nature. 2014;505:691–5.
35. Cui S, Yu Q, Chu L, Cui Y, Ding M, Wang Q, et al. Nuclear cGAS functions non-canonically to enhance antiviral immunity via recruiting methyltransferase Prmt5. Cell Rep. 2020;33:108490.
36. Yang H, Wang H, Ren J, Chen Q, Chen ZJ. cGAS is essential for cellular senescence. Proc Natl Acad Sci USA. 2017;114:E4612–e20.
37. Kwon J, Bakhoum SF. The cytosolic DNA-sensing cGAS-STING pathway in cancer. Cancer Discov. 2020;10:26–39.
38. Wang H, Hu S, Chen X, Shi H, Chen C, Sun L, et al. cGAS is essential for the antitumor effect of immune checkpoint blockade. Proc Natl Acad Sci USA. 2017;114:1637–42.
39. Gracilla DE, Korla PK, Lai MT, Chiang AJ, Liou WS, Sheu JJ. Overexpression of wild type or a Q311E mutant MB21D2 promotes a pro-oncogenic phenotype in HNSCC. Mol Oncol. 2020;14:3065–82.
40. Xu H, Li H, Woo SL, Kim SM, Shende VR, Neuendorff N, et al. Myeloid cell-specific disruption of Period1 and Period2 exacerbates diet-induced inflammation and insulin resistance. J Biol Chem. 2014;289:16374–88.
41. Sanjana NE, Shalem O, Zhang F. Improved vectors and genome-wide libraries for CRISPR screening. Nat methods. 2014;11:783–4.
42. Wang P, Zhao W, Zhao K, Zhang L, Gao C. TRIM26 negatively regulates interferon-β production and antiviral response through polyubiquitination and degradation of nuclear IRF3. PLoS Pathog. 2015;11:e1004726.

ACKNOWLEDGEMENTS

This work was supported by grants from National key research and development program (2021YFC2300603) and the National Natural Science Foundation of China (32230033, 81930039, 31730026).

AUTHOR CONTRIBUTIONS

CG conceived and supervised the study. HL, ZY and DZ performed the experiments. HX, FL, TC, H.Z, YZ, BL, LZ and WZ contributed to experimental design and discussion. HL, ZY and DZ analyzed the data. ZY, HL and CG wrote the manuscript.

COMPETING INTERESTS

The authors declare no competing interests.

ETHICS APPROVAL

All animal studies were approved by the Scientific Investigation Board of School of Basic Medical Science, Shandong University (ECSBMSSDU2020-2-072).

ADDITIONAL INFORMATION

Supplementary information The online version contains supplementary material available at https://doi.org/10.1038/s41418-023-01116-1.

Correspondence and requests for materials should be addressed to Chengjiang Gao.

Reprints and permission information is available at http://www.nature.com/reprints

Publisher's note Springer Nature remains neutral with regard to jurisdictional claims in published maps and institutional affiliations.